2004

A Chandra ACIS View of the Thermal Composite Supernova Remnant 3C 391

Y Chen

Y Su

PO Slane

QD Wang
University of Massachusetts - Amherst, wqd@astro.umass.edu

A *Chandra* ACIS view of the Thermal Composite Supernova Remnant 3C 391

Yang Chen[1,2], Yang Su[1], Patrick O. Slane[3], and Q. Daniel Wang[2]

ABSTRACT

We present a 60 ks *Chandra* ACIS-S observation of the thermal composite supernova remnant 3C 391. The southeast-northwest elongated morphology is similar to that previously found in radio and X-ray studies. This observation unveils a highly clumpy structure of the remnant. Detailed spatially resolved spectral analysis for the small-scale features reveals that the interior gas is generally of normal metal abundance and has approached or basically reached ionization equilibrium. The hydrogen column density increases from southeast to northwest. Three mechanisms, radiative rim, thermal conduction, and cloudlet evaporation, may all play roles in the X-ray appearance of 3C 391 as a "thermal composite" remnant, but there are difficulties with each of them in explaining some physical properties. Comparatively, the cloudlet evaporation model is favored by the main characteristics such as the highly clumpy structure and the uniform temperature and density distribution over most of the remnant. The directly measured postshock temperature also implies a young age, $\sim 4 \times 10^3$ yr, for the remnant. The postshock gas pressure derived from the NE and SW rims, which harbor maser spots, is consistent with the estimate for the maser regions. An unresolved X-ray source is observed on the northwest border and its spectrum is best fitted by a power-law.

1. Introduction

3C 391 (G31.9+0.0), a supernova remnant (SNR) with irregular morphology, has been observed in several electromagnetic bands. Radio observations with the VLA reveal an elongated structure extending from the northwest (NW) to the southeast (SE), surrounded

[1]Department of Astronomy, Nanjing University, Nanjing 210093, P.R.China

[2]Department of Astronomy, B619E-LGRT, University of Massachusetts, Amherst, MA01003

[3]Harvard-Smithsonian Center for Astrophysics, Cambridge, MA 02138

by a shell except on the SE border, where it appears that the SNR has broken out of a dense region into an adjacent region of lower density (Reynolds & Moffett 1993). In X-rays, both *Einstein* (Wang & Seward 1984) and *ROSAT* (Rho & Petre 1996) observations show that the centroid of the soft X-ray emission sits in the SE region. The *ASCA* observation reveals a hard X-ray enhancement in the NW region, and confirms the decrease in hydrogen column density across the remnant from NW to SE (Chen & Slane 2001). Two hydroxyl radical 1720 MHz maser spots are found along the radio shell (Frail et al. 1996). The masers and the strong enhancement in [OI] 63μm emission near the northwestern edge (Reach & Rho 1996) both provide evidence for shock interactions with a molecular cloud. CO and other molecular line observations place the location of the remnant at the southwestern (SW) edge of a molecular cloud (Wilner, Reynolds, & Moffett 1998; Reach & Rho 1999).

3C 391 is an example of the "thermal composite" or "mixed morphology" category of supernova remnants, which also includes W28, W44, IC 443, G349.7+0.2, and others (Rho & Petre 1998). They generate bright *thermal* X-ray emission interior to their radio shells, and have faint X-ray rims. They are usually found to interact with adjacent molecular clouds, characterized by the hydroxyl radical maser emission (Green et al. 1997, Yusef-Zadeh et al. 2003). Non-thermal diffuse X-ray emission inside SNRs is widely believed to be synchrotron radiation from pulsar wind nebulae, while the nature of the internal thermal X-ray emission seen in mixed morphology remnants is still uncertain.

At least four distinct scenarios have been proposed to explain centrally-brightened X-ray morphology. The first scenario is radiative cooling of the rim gas. Under this hypothesis, the gas at the rim has been cooled down in the radiative stage of evolution, with a temperature so low ($< 10^6$ K) that its X-ray emission is very weak, while the gas in the inner volume is still hot enough to emit strong X-rays (e.g. Harrus et al. 1997, Rho & Petre 1998).The second mechanism invokes thermal conduction. It is suggested that thermal conduction in the remnant can smooth out the temperature gradient from the hot interior to the cooler shell, and increase the central density in response to the associated change in pressure conditions. This results in luminous X-rays in the interior, and is dominant in the radiative stage (Cox et al. 1999, Shelton et al. 1999). The third scenario invokes cloudlet evaporation in the SNR interior. When a SNR expands in an inhomogeneous interstellar medium (ISM) whose mass is mostly contained in small clouds, the clouds engulfed by the blast wave can be evaporated to slowly increase the density of the interior gas; as a result, the SNR appears internally X-ray brightened (White & Long 1991). The fourth suggestion is that the mixed morphology is a projection effect. For shell-like SNRs that evolve in a density gradient such as at the edge of a molecular cloud, if the line of sight is essentially aligned with the density gradient as well as the magnetic field, the SNRs will appear as thermal composites (Petruk 2001).

To date, X-ray studies have not yet provided strong evidence favoring any one of these mechanisms. Here we report on high resolution *Chandra* observations of 3C 391 aimed at addressing the nature of the centrally filled X-ray emission in this SNR.

2. Observation and Data Analysis

We observed SNR 3C 391 with the Advanced CCD Imaging Spectrometer (ACIS) on board the *Chandra* X-ray observatory on 03 August 2002 (Obs. ID 2786) for an exposure of 62 ks. The target center ($18^h49^m28^s.3$, $-00°56'15''$) was placed $\sim 2'$ off the telescope aim-point for an optimal coverage of the supernova remnant on the S3 (#7) CCD chip (using very faint mode).

The level 1 raw event data were reprocessed to generate a new level 2 event file to capitalize on the Chandra Interactive Analysis of Observations (CIAO) software package (version 2.3). In the reprocessing, bad grades have been filtered out and good time intervals have been reserved. We also removed time intervals with significant background flares (peak count rates $\gtrsim 3\sigma$ and/or a factor of $\gtrsim 1.2$ off the mean background level of the observation). This cleaning, together with a correction for the dead time of the observation, resulted a net 60.7 ks exposure for subsequent analysis. Furthermore, a correction was made for the time-dependence of the ACIS gain.

2.1. Spatial Analysis

For imaging analysis, we produced exposure maps in 0.3-1.5, 1.5-3.0, and 3.0-7.0 keV bands. These maps were used for flat-fielding, accounting for bad pixel removal as well as correcting for telescope vignetting and the quantum efficiency variation across the detector. The images in the three bands are adaptively smoothed (using CIAO tool *csmooth* with signal-to-noise ratio of 3) and exposure-corrected. The tri-color X-ray image (0.3-1.5 keV in red, 1.5-3.0 keV in green, and 3.0-7.0 keV in blue), overlaid with the 1.5 GHz radio contours (from Moffett & Reynolds 1994), is shown in Fig.1a. Another tri-color image with 1.5 GHz emission in red, 0.3-3.0 keV in green, and 3.0-7.0 keV in blue is shown in Fig.1b. A broad band (0.3-7.0 keV) image overlaid with the radio contours are shown in Fig.1c. The two OH maser points (Frail et al. 1996) are labeled in these three maps.

We searched for point-like sources in three broad bands, 0.3-1.5 keV (S), 1.5-7.0 keV (H), and 0.3-7.0 keV (B). A combination of source detection algorithms were applied: wavelet, sliding-box, and maximum likelihood centroid fitting (see Wang, Chaves, & Irwin 2003 for

details of the approach). The estimation of the count rate of a source was based on the data within the 90% energy-encircled radius (EER) determined with the calibrated point spread function of the instrument. The information obtained for the point-like sources detected this way on the S3 chip are summarized in Table 1.

In order to produce a map of diffuse emission, we removed the point-like sources with each source region as a circle of twice the 90% EER. After filling the source-removed "holes" (in a swiss-cheese-like map) by interpolating the intensity from the surrounding regions, we produced a smoothed (with count-to-noise ratio of 6), exposure-corrected diffuse X-ray map in 0.3-7 keV (Fig.1d). Also shown in Fig.1d are the regions used for spectral fitting (see §2.2).

These X-ray images display the SE-NW elongated morphology, similar to that observed in the earlier radio (Moffett, & Reynolds 1994) and X-ray (Rho & Petre 1996, Chen & Slane 2001) observations, but with considerable small-scale structure revealed by the superb angular resolution of *Chandra*.

The X-ray maps reveal a highly clumpy structure of the remnant, with clumps or knots located in both the SE and NW parts. A bright hard enhancement is peaked at $(18^h49^m27^s.0, -00°54'10'')$ near the the NW border (see Fig.1a); this corresponds to region #3 in Fig.1d. A complex mixture of knots is seen in the SE part of the remnant interior, including at least four bright enhancements in all colors centered at $\sim (18^h49^m29^s.3, -00°56'42'')$ (region #6), $(18^h49^m32^s.9, -00°56'58'')$ (region #7), $(18^h49^m35^s.5, -00°57'04'')$ (region #8), and $(18^h49^m29^s.8, -00°57'45'')$ (region #9). Similar clumpy structures are also seen in the interior of SNR N49B (Park et al. 2003). Several remarkable, very bright knotty features appear on the east and SE border of 3C 391. Also, the eastern knot seems to coincide with the location of the infrared source IRAS 18470-0100 (whose fluxes are 1.32, 4.66, 23.8, and 236 Jy at 12, 25, 60, and 100 μm, respectively). These bright knots on the border may be small clouds that have recently been shocked by the supernova blast wave.

In the RGB 3-color map Fig.1a, yellow and light-green colors indicate strong soft emission in the SE part, while fainter soft emission appears brown in color and is seen in the middle section of the elongated body of the remnant. A faint arc appears in the rim of the northern brown patch. This arc/shell seems to connect with another shell like structure at the northeastern (NE) rim, which is evident in radio (Fig.1b) and discernible in X-rays, and harbors one of the previously detected OH masers (Frail et al. 1996). On the opposite side, no shell-like X-ray structure can be discerned along the southern and SW border, but faint diffuse X-ray emitting gas seems to spill outside the radio border in the southwest.

In Fig.1a, the green color representing the middle-band emitting gas almost pervades

the whole postshock region of the NW part. The pervasive green color in the NW, mixed with a small blue patch, shows hardening of the X-ray spectrum. This is consistent with gradual increase in hydrogen column density across the remnant (Chen & Slane 2001; see also §3.2 below).

The radio contour overlays make it very apparent that there is a shock interaction with a molecular cloud on the NW border because of the flat morphology of the radio emission. At the west rim, a soft X-ray brightened slab appears to be very close to (just slightly behind) the radio peak emission (region #12), and may be related to a small dense region there.

A few point sources are seen in the remnant's geometric center and the south and west portions (Fig.1 and Table 1). The small number of counts collected make it difficult to determine their nature. A bright hard enhancement ($18^h49^m22^s.3, -00°53'34''$) appears as an unresolved source on the NW border (source #17 in Table 1; region #5 in Fig.1d). We discuss the spectrum of this source below (§3.3.).

2.2. Spectral Analysis

Taking advantage of *Chandra*'s superb angular resolution, we have performed the spatially-resolved spectral analysis of 3C 391. Prior to the extraction of spectra, we removed the point-like sources detected on the S3 chip (see Table 1) except for weak sources with $\log(P) > -9.0$ (see Table 1 for the detailed definition of the false detection probability P) and those with a high possibility of being clumps of diffuse emission (judged by eye). We defined 13 small-scale regions, 3 medium-scale regions, and the region of the entire remnant (as diagramed in Fig.1d) for spectral investigation. Most of the small-scale regions are chosen to include the small features of X-ray enhancement such as the knots and the faint shell like structures. Two medium-size circles are used to compare the mean spectral variation between the inner SE and NW portions. The remaining area on the S3 chip outside region #17 for the entire remnant was used for background. For each chosen region, we use the CIAO script *acisspec* to extract the spectrum and obtain the weighted response matrix. The net count rates of these extracted spectra are tabulated in Table 2 and Table 3. Corrections for the continuous degradation in the ACIS quantum efficiency have been applied to auxiliary response files. All the spectra mentioned above were regrouped to contain at least 25 net counts per bin.

There are three distinct line features, Mg Heα ($\sim 1.35\,\text{keV}$), Si Heα ($\sim 1.85\,\text{keV}$), and S Heα ($\sim 2.46\,\text{keV}$) in these spectra except the spectrum of a NW unresolved source (region #5), confirming their thermal origin (see Fig. 2 and Fig. 3). The Fe L complex could have significant contribution in the range $\sim 0.5\text{-}1.5\,\text{keV}$. The emission diminishes rapidly above

the photon energy $\sim 5\,\mathrm{keV}$ and no Fe Kα emission is observed.

Using the Morrison & McCammon (1983) interstellar absorption, we test to fit the thermal spectra with various collisional equilibrium ionization and non-equilibrium ionization (NEI) models for the optically thin plasma of SNRs available in the XSPEC code. We find that our spectra can be best described by the VNEI model with NEI spectral version 2.0, which uses the Astrophysical Plasma Emission Database (APED) to calculate spectrum [1]. Considering the evident line emission from Mg, Si, S, and possibly Fe L, we treat the abundances of these element species as free parameters. In most cases, however, thawing the abundances did not significantly improve the spectral fit relative to that using solar abundances. For a few cases, especially for the emission from medium-scale regions and from the entire remnant, thawing the abundances do indeed improve the fitting. The spectral fit results are tabulated in Table 2. The spectrum of the NW unresolved source (region #5) can be best fitted with an absorbed power-law emission (see the spectral fit parameters summarized in Table 3) and cannot be fitted with a blackbody emission.

The spectral fits show that the diffuse emission from various regions have ionization parameters ($n_e t$) close to or higher than $10^{12}\,\mathrm{cm^{-3}\,s}$. This implies that the hot plasma in the SNR is very close to, or is basically in, the ionization equilibrium.

The spectral fits also show that the diffuse emission from small-scale regions can be well fitted with solar abundances, and the emissions from larger regions can be fitted with abundances very close to solar values.

The temperature of the gas interior to the SNR is $\sim$0.5-0.6 keV, with only small fluctuations. For instance, the lowest temperature ($\sim 0.46\,\mathrm{keV}$) is found at the faint SE rim (region #13), and the highest temperature ($\sim 0.8\,\mathrm{keV}$) is seen at the NE rim (region #10).

The absorption column density is found to generally increase across the remnant from SE to NW. This is consistent with the conclusion of the *ROSAT* (Rho & Petre 1996) and *ASCA* studies (Slane & Chen 2001), and is also consistent with the emission hardening shown in the previous section. The absorption in the SE part is about $\sim 2.9 \times 10^{22}\,\mathrm{cm^{-2}}$ (region #14). The highest absorption ($\sim 4.1 \times 10^{22}\,\mathrm{cm^{-2}\,s^{-1}}$) is found in a NW region (region #4) which is in blue in the tri-color image (Fig.1a). This hardest region was also seen in the *ASCA* study (see Fig.3 in Chen & Slane 2001). A very high absorption ($\sim 3.7 \times 10^{22}\,\mathrm{cm^{-2}\,s^{-1}}$) is also found at the westmost rim (region #12). The difference of mean N_{H} between the central SE region (region #14) and the central NW region (region #15) is $\sim 6 \times 10^{21}\,\mathrm{cm^{-2}}$. Such a variation in N_{H} is consistent with the existence of a molecular cloud to the NW (Wilner et

---

[1] http://cxc.harvard.edu/atomdb/sources.html

al. 1998; Reach & Rho 1999).

3. Discussion

Similar to the hydrogen column density distribution across the remnant obtained in previous X-ray studies, the N_{H} values obtained in the spectral analysis are confirmed to increase from the SE toward the NW. The spatial analysis also shows an obvious spectral hardening in the NW part. This could naturally be explained by the scenario that the NW part of the remnant is embedded in the molecular cloud (Reynolds & Moffett 1993). The mean difference of N_{H} between the SE and NW interior portions, $\sim 6 \times 10^{21} \, \mathrm{cm}^{-2}$, is consistent with that found in the *ASCA* study, and implies a mean density of the ambient molecular gas $\langle n(\mathrm{H_2}) \rangle$ of order $\sim 10\text{-}20 \, \mathrm{cm}^{-3}$ on the assumption that the SNR line-of-sight depth in the cloud is similar to the remnant radius (Chen & Slane 2001). We also adopt the distance $d \sim 8 d_8 \, \mathrm{kpc}$ estimated there.

According to the NEI fit to the spectrum of the entire remnant (region #17), the X-ray luminosity in 0.5–10 keV of the remnant is $L_X = 3.5 \times 10^{36} d_8^2 \, \mathrm{ergs \, s^{-1}}$. From the volume emission measure $f n_e n_{\mathrm{H}} V \sim 1.5 \times 10^{59} d_8^2 \, \mathrm{cm}^{-3}$, where f is the filling factor of the X-ray emitting gas, the mean number density of the gas interior to the remnant is $1.9 f^{-1/2} d_8^{-1/2} \, \mathrm{cm}^{-3}$ (here $n_e \approx 1.2 n_{\mathrm{H}}$ has been used and a cylinder-like volume of a diameter $5'$ and a height $7'$ has been assumed). The remnant volume is $V \sim 5.1 \times 10^{58} d_8^3 \, \mathrm{cm}^{-3}$. The mass of the X-ray emitting gas is $M_x \sim 1.4 n_{\mathrm{H}} m_{\mathrm{H}} f V \sim 114 f^{1/2} d_8^{5/2} M_\odot$.

Raw estimates for the gas density of the regions used for spectral fit (apart from #17, the entire remnant) can also be given in terms of the volume emission measures. We assume that the circular regions correspond to spheres, the elliptical regions to oblate spheroids, and the rectangular regions to shell structures. The gas densities thus obtained are listed in the last column of Table 2. The densest X-ray emitting gas is located in the SE and eastern regions #1 and #2 that contain very bright knots (with density $\gtrsim 10 f^{-1/2} d_8^{-1/2} \, \mathrm{cm}^{-3}$). The other bright knots (regions #3 in the NW and #6, #7, #8, and #9 in the inner central SE portion) have a gas density $\sim 5\text{-}7 f^{-1/2} d_8^{-1/2} \, \mathrm{cm}^{-3}$. The regions along the remnant border (#10, #11, #12, #13, and #16) have a density $\sim 1\text{-}3 f^{-1/2} d_8^{-1/2} \, \mathrm{cm}^{-3}$.

3.1. Origin of centrally-filled X-ray morphology and dynamics of the remnant

As mentioned in the Introduction, four main mechanisms have been proposed to explain the X-ray morphology of thermal composite SNRs: projection effect, radiative shells, thermal

conduction, and cloudlet evaporation. Here we compare them with the properties found from our spatially-resolved spectral analysis.

3.1.1. Projection effect

The projection effect does not match the properties found in 3C 391. As mentioned above, the molecular cloud is located in the NW but the X-ray emission is not only enhanced in the NW half, but also in the SE half. Moreover, the hydrogen column density increases along the SE-NW elongation direction, so the density gradient of the ambient medium seems to be close to the projection plane, and hence will make the projection effect weak according to the Petruk (2001) model.

3.1.2. Radiative rim

Though there is no report in the available literature of the presence of an HI shell around the remnant like that in W44, another thermal composite SNR (Koo & Heiles 1995), the diffuse filamentary near-infrared [Fe II] and the mid-infrared 12-18 μm [Ne II] and [Ne III] emission along the NW radio shell provide some evidence for a radiative cooling at the rim (Reach, Rho, & Jarrett 2001). As viewed in Fig.1, the volume of the remnant as delineated by the radio shell (including the regions of the near- and mid-infrared emission) is basically filled with X-ray emitting gas. Several examined portions of X-ray emission on the borders, such as the NE rim (region #10), the northern rim (region #11), the western rim (region #12), the SW faint rim (region #16), and the SE rim (region #13), which should be dominated by the postshock gas of the supernova blast wave (and are indeed located at the edge of the radio shell), are found to be at temperatures higher than 5×10^6 K. This indicates that a considerable amount of gas at the blast shock has not yet suffered heavy radiative cooling, and is capable of generating considerable X-ray emission along the remnant's border. If the gas density of these regions, ~ 1–$3 f^{-1/2} d_8^{-1/2}$ cm^{-3}, is approximated as the postshock density, then the preshock intercloud medium (ICM) has a density about 0.2–$0.7 f^{-1/2} d_8^{-1/2}$ cm^{-3}.

According to the infrared spectroscopic study, the ambient environment in the NW part has complicated physical properties, with at least three typical preshock components (Reach & Rho 2000). For the atomic component implied by the [OIII] and [NIII] emission, the preshock density $n_0 < 1$ cm^{-3} and the shock velocity $v_s \sim 500$ km s^{-1}; for the moderate-density molecular component revealed by the [OI], [SiII], and [FeII] emission, the gas density $n_{cl} \sim 10^2$ cm^{-3} and the shock velocity $v_{cl} \sim 10^2$ km s^{-1}; and for the dense clumps giving

rise to H_2, OH, CO, CS, and H_2O molecular emission, the gas density $\sim 10^4\,\mathrm{cm^{-3}}$ and the shock velocity $\sim 20\,\mathrm{km\,s^{-1}}$. Thus there may be two possibilities about the coexistence of the radiative filaments and the X-ray emitting gas along the NW rim: 1) the cooling shell may be in the early stage of its formation; or 2) the radiative filaments may be caused by the propagation of the shock waves into some regions of higher density in the molecular cloud so that these regions of postshock gas have cooled down severely while most of the gas at the rim is still hot.

In the first case, we note that the bright [FeII] emission coincides precisely with the brightest radio bar along the western border, which is regarded as the interface between the remnant and the molecular cloud (Reach, Rho, & Jarrett 2001), and that, as we find here, the soft X-ray brightened slab along the west border (in region #12) appears to be very close to, but slightly behind, the radio bar. The shell formation time can be estimated according to $t_{\mathrm{shell}} \approx 5.3 \times 10^4 (E_{51}^{3/14}/n_0^{4/7})$ yr (Cox et al. 1999). If the mean preshock hydrogen nucleus density is $n_0 \sim 30\,\mathrm{cm^{-3}}$ (twice the molecular density $\langle n(H_2)\rangle \sim 10\text{-}20\,\mathrm{cm^{-3}}$ given above), $t_{\mathrm{shell}} \approx 7.6 \times 10^3 E_{51}^{3/14}$ yr; if the preshock density is $n_0 \sim 100\,\mathrm{cm^{-3}}$ for the moderately dense cloud, $t_{\mathrm{shell}} \approx 3.8 \times 10^3 E_{51}^{3/14}$ yr. The remnant's age would not be much larger than these estimates.

In the second case, the blast shock propagates in an inhomogeneous medium. After a blast shock impacts a cloud, a transmitted shock (at velocity v_{cl}) is expected to move into the cloud. The pressure balance between the shocked cloud and the shocked ICM gives $n_{cl}v_{cl}^2 = \beta n_{icm}v_s^2$, where factor $\beta \sim 1$ for a shock interaction with small clouds (McKee & Cowie 1975) and $\beta \approx 4.4$ and 6 for a strong shock hitting a rigid cloud plane for $n_{cl}/n_0 = 100$ and ∞, respectively (Zel'dovich & Raizer 1967). The moderate-density ($n_{cl} \sim 100\,\mathrm{cm^{-3}}$) cloud may, after it is shocked (with $v_{cl} \sim 100\,\mathrm{cm^{-3}}$), be responsible for the filamentary near- and mid-infrared emission and the tenuous atomic component ($n_{icm} < 1\,\mathrm{cm^{-3}}$) may, after shocked, correspond to the postshock X-ray emitting gas detected by *Chandra*. For the western X-ray slab ($kT \sim 0.6\,\mathrm{keV}$) along the radiative filaments, the velocity of the blast wave in the hot gas is $v_s = (16kT/3\mu m_{\mathrm{H}})^{1/2} \sim 700\,\mathrm{km\,s^{-1}}$ (where the mean atomic weight $\mu = 0.61$), and the preshock density is $n_{icm} = n_{\mathrm{H}}/4 \sim 0.5\,\mathrm{cm^{-3}}$. Thus we have $\beta \sim 4.1 f^{1/2}d_8^{1/2}$, which suggests that the SNR shock wave hits the plane surface of a dense cloud. This is consistent with the flat morphology of the NW radio bar.

3.1.3. Thermal conduction

The spatially-resolved spectral analysis demonstrates that the hot gas over most interior regions of the SNR is at similar temperatures of around 0.5-0.6 keV. Such a uniform distri-

bution of the gas temperature inside the remnant is not consistent with the canonical Sedov distribution in which the inner temperature is higher than that near the rim. On the other hand, the X-ray morphology of this remnant is not limb brightened, and this is inconsistent with the Sedov solution as well. Cox et al. (1999) explain this sort of morphology (as observed in W44) in terms of the effect of thermal conduction of the interior gas, which could prevent the formation of a hot vacuous cavity described by the adiabatic Sedov solution and provide enough material in the center to make it bright in X-rays.

The thermal conduction scenario could apply to 3C 391 to some extent. If the suppression of conduction by magnetic fields can be ignored, the conduction timescale would be $t_{\rm cond} \sim n_e k \ell^2 / \kappa$, where ℓ denotes the linear scale of the temperature gradient and the conductivity is given by $\kappa = 1.84 \times 10^{-5} T^{5/2} / \ln \Lambda \, {\rm ergs \, s^{-1} \, K^{-1} \, cm^{-1}}$ with the Coulomb logarithm $\ln \Lambda = 29.7 + \ln n_e^{-1/2} (T/10^6 \, {\rm K})$ (Spitzer 1962). If ℓ is taken to be of order the remnant's mean radius 7 pc, the timescale would be $t_{\rm cond} \sim 4.7 \times 10^4 \, {\rm yr}$, much larger than the remnant's inferred age. It would, however, be much smaller than this in the early stage of the evolution in which T would be higher and ℓ would be smaller. If we look at small spatial scales of order the separation between clumps (typified by $1' \sim 2.3 \, {\rm pc}$), the timescale would be $5.2 \times 10^3 \, {\rm yr}$, comparable to the remnant's age (see §3.1.4.), and hence thermal conduction may play a role in smoothing of the interior temperature profile. We note that X-ray clumps are also present in W44 (Shelton, Kuntz, & Petre 2004) where thermal conduction may be an efficient mechanism. The fact that the hot gas in 3C 391 is near ionization equilibrium suggests that there may be relatively little newly shocked material and is consistent with the idea of some mechanism smoothing the properties. More significantly, the presence of the radiative filaments along the NW border is also in favor of the thermal conduction model.

There are, however, disagreements in the distribution of physical properties between the observation and the model interpretation. In the thermal conduction scenario in which a centrally brightened X-ray morphology is reproduced (Cox et al. 1999, Shelton et al. 1999), the central pressure is about 0.3 of that at the edge and the central density would be about much lower (0.13 times at radiative shell formation) than the preshock ICM density, but this is not consistent with the case of 3C 391. In fact, this remnant has a uniform temperature around 0.5-0.6 keV throughout and the inner mean density $\sim 3 f^{-1/2} d_8^{-1/2} \, {\rm cm^{-3}}$ (regions #14 and #15) is not smaller than the hot gas density ~ 1–$3 f^{-1/2} d_8^{-1/2} \, {\rm cm^{-3}}$ along the periphery. In the model the temperature would be expected to decrease gradually away from the inner portions to the outer. Unlike W44 in which the gas temperature is found to drop by a factor $\lesssim 2$ between the center and $\sim 6 \, {\rm pc}$ from the center (Shelton et al. 2004), in 3C 391 our measurement does not suggest the temperature decrease even if the line-of-sight projection is taken into account. The inner temperature is not higher than the gas temperature in most portions along the rim, and highest temperatures appear at a location on the border (region

#10, the NE rim).

·

3.1.4. Cloudlet evaporation

The phenomenon of low temperature in the inner portions could result from substantial cloudlet evaporation because part of the thermal energy is deposited to the gas evaporated from the cold cloudlets. The relatively uniform distribution of temperature (even with slightly lower values at the center) is actually expected by the White & Long (1991) cloudlet evaporation model for model parameters $\tau \to \infty$ and $C/\tau \gtrsim 3$ (see Fig.2 and Fig.4 therein), where τ is the ratio of the cloud evaporation timescale to the SNR's age and C is the ratio of the mass in the cloudlets to the mass of ICM. The ratio between the mean density ($\sim 2f^{-1/2}d_8^{-1/2}\,\mathrm{cm}^{-3}$) and the density along the border (~ 1–$3f^{-1/2}d_8^{-1/2}\,\mathrm{cm}^{-3}$) is basically consistent to that predicted in the evaporation model. In fact, the highly clumpy structure unveiled in this observation lends support to the conjecture that the ambient molecular cloud is inhomogeneous. The cloudlets engulfed by the supernova blast wave can act as a large reservoir of interior gas by gradual evaporation. This could also explains why the mean density of the hot gas inside the remnant (as mentioned above) is much lower than that of the ambient cloud gas. The association between the thermal composites and the OH maser emission in molecular clouds is strongly suggestive of the role played by clouds in the SNRs (Yusef-Zadeh et al. 2003).

With a little adjustment of the model parameters used in the *ASCA* study of 3C 391 (Chen & Slane 2001, see Table 6 therein), we here adopt $C/\tau \sim 3$–6. Using the temperature measured from the entire remnant (region #17) $kT_X \approx 0.56\,\mathrm{keV}$ as the average temperature, the White & Long (1991) model would predict a postshock temperature 0.46–0.64 keV, consistent with most of the postshock temperatures measured from the spectral analysis. The velocity of the blast wave is $v_s = (16kT_s/3\mu m_{\mathrm{H}})^{1/2} \sim 620$–$730\,\mathrm{km\,s^{-1}}$ (where the mean atomic weight $\mu = 0.61$). Adopting a mean radius of the remnant $r_s = 3'r_3 \sim 7.0r_3 d_8$, we estimate the dynamical age of the remnant: $t = 2r_s/5v_s \sim 3.7$–$4.4 \times 10^3 r_3 d_8\,\mathrm{yr}$. Because our *Chandra* observation can measure the postshock temperature of 3C 391, this age estimate should be more accurate than those obtained from *ROSAT* and *ASCA* observations using the same model, and the age of remnant is somewhat smaller than previously thought. The preshock gas density ($n_0 \sim 0.2$–$0.7f^{-1/2}d_8^{-1/2}\,\mathrm{cm}^{-3}$) estimated above could be regarded as the preshock ICM density. An alternative estimate of the preshock ICM density is obtained from the remnant's X-ray luminosity ($L_X = 3.5 \times 10^{36}d_8^2\,\mathrm{ergs\,s^{-1}}$): $n_0 \sim 0.07$–$0.4\,\mathrm{cm}^{-3}$ by use of eq.(21) in White & Long's (1991) model. According to this model, the explosion energy of the supernova remnant is $E = [16\pi(1.4n_0 m_{\mathrm{H}})/25(\gamma+1)K](r_s^5/t^2) \sim 0.3$–

$1.4 \times 10^{51} r_3^3 d_8^3 (n_0/0.3 \, \mathrm{cm}^{-3})$ ergs (where the adiabatic index $\gamma = 5/3$ and the ratio of thermal to kinetic energy $K \sim 0.385$–0.132).

The application of the evaporating cloudlets model to 3C 391 may raise a few questions, which are discussed below and need further clarification.

First, the remnant ages may be systematically underestimated by the White & Long model for a given explosion energy. W44 is a typical example, where an age of $\sim 7 \times 10^3$ yr estimated from the evaporation model (Rho et al. 1994) is smaller than the spindown time scale $\sim 2 \times 10^4$ yr of the associated pulsar (Wolszczan, Cordes, & Dewey 1991). The age derived above for 3C 391 ($\sim 4 \times 10^3 r_3 d_8$ yr) using the evaporation model may possibly be an underestimate. If a Sedov evolution is adopted, the postshock temperature $kT_s \sim 0.6$ keV would correspond to a similar age $2r_s/5v_s \sim 4 \times 10^3 r_3 d_8$ yr; as a comparison, Reynolds & Moffett (1993) present an estimate $\sim 1.7 \times 10^4 E_{51}^{-1}$ yr for a cloud density $n_0 \sim 100 \, \mathrm{cm}^{-3}$. Considering the possibility of the SNR being in the radiative phase, Chen & Slane (2001) obtain an age $\sim 1.9 \times 10^4 E_{51}^{31/42} (r_3 d_8)^{10/3}$ yr for a preshock density $n_0 \sim 30 \, \mathrm{cm}^{-3}$.

Second, the cloudlet evaporation scenario needs a model parameter $\tau \rightarrow \infty$ (with $C/\tau \gtrsim 3$), and thus the influence of cloud evaporation on the properties of the interior gas seems possibly negligible. Similar parameters are required to explain the X-ray morphology of another thermal composite MSH11-61A observed with *ASCA* (Slane et al. 2002). In contrast, hydrodynamic simulations (e.g., Xu & Stone 1995, using a density contrast $\chi = 10$) show that clouds tend to get disrupted soon after passing through a strong shock. In our observation of 3C 391, however, the SE bright knots (in region #1) appear compact and survive the shock passage. The ratio of the hot gas density of these knots to the mean density of the entire remnant is about 10 (see Table 2), so it would be reasonable to assume that the cloud-to-ICM density contrast χ is much higher than this number or to assume a high mass contrast C. The other X-ray knots interior to the remnant may also be the dense regions that have not been destroyed by the blast shock. The denser clouds could be expected to survive longer time, and still a large amount of dense matter expected to have not been evaporated from cloudlets yet. Infrared observations of 3C 391 have detected dense ($\gtrsim 10^4 \, \mathrm{cm}^{-3}$) molecular clumps in the southwest "broad molecular line" region, each H_2 clump being of size ~ 0.1 pc (Reach & Rho 1999, Reach & Rho 2000, Reach et al. 2002). (As a comparison, the compact SE knots in region #1 are of size ~ 0.5 pc.) It is not impossible that the X-ray knots contain similar dense cloudlets.

Third, if the bright knots stands for the newly evaporated cloud material, it should have been seen cooler than the mean temperature. Nonetheless, because the evaporated gas would be soon heated up to the environmental temperature about 2 times the cloud radius from the cloud (Cowie & McKee 1977), the spectral properties of the cooler component could

be smoothed out if the knots are much larger than the cold cloudlets (for instance, 0.5 pc versus 0.1 pc as described above).

Fourth, the newly evaporated gas should have a low ionization age. The knots in regions #2, #6, #7, #8, and #9 marginally satisfy this condition ($\gtrsim 10^{11}$ s), especially if the evaporated gas had been pre-ionized by the ultraviolet photons and/or the transmitted shock wave, while those in region #1 has a high ionization age ($> 10^{12}$ s). The latter case does not satisfy the condition, unless, again, the low ionization age could be smeared by the surrounding gas if the cold clouds are very small.

Concluding this section, we suggest that three mechanisms, radiative rim, thermal conduction, and cloudlet evaporation, all play roles in the inner brightened X-ray morphology of 3C 391. By comparison, the cloudlet evaporation can largely explain some important properties such as the highly clumpy structure, the uniform temperature and density distribution almost all over the remnant, and the much lower X-ray emitting gas density than the mean ambient cloud density. Nonetheless, even cloudlet evaporation is driven by saturated conduction. It is probably true in many thermal composite remnants, and in 3C 391 as well, that the morphology arises from a combination of expansion into an inhomogeneous medium and heat conduction on various scales.

3.2. Maser spots

As in many other thermal composites, hydroxyl radical 1720 MHz maser spots are found within 3C 391. The two maser spots are located on the radio shell (Frail et al. 1996), one of which is here found to be harbored in the NE rim (region #10) where X-ray emission is modestly enhanced at a high plasma temperature (~ 0.8 keV) and the other of which is in the southwest region (#16) where the X-ray emission is faint (see Fig.1).

The OH (1720 MHz) maser spots are believed to be due to C-type shock collisional excitation in the clumpy molecular clouds, with cloud temperature and density conditions $50 \leq T \leq 125$ K and $10^4 \leq n_{\mathrm{H_2}} \leq 5 \times 10^5$ cm^{-3} (Elitzur 1976; Lockett, Gauthier, & Elitzur 1999). The production of OH molecules is enhanced by the X-ray emission (with an ionization rate $\gtrsim 10^{-16}$ s^{-1}) behind the C-shock (Wardle 1999).

According to Wardle's model formula, the X-ray induced ionization rate in the post-shock regions of 3C 391 is about 2×10^{-15} s^{-1} (using the X-ray luminosity $L_X \sim 2.3 \times 10^{36}$ ergs s^{-1} and the mean radius ~ 7 pc), well above the rate needed for the OH enhancement. Let us take the X-ray enhanced region #10 and X-ray faint region #16 as oblate spheroids. Thus the volume in region #10 is $\sim 6.3 d_8^3$ pc^3 and the mean gas density is

$\sim 2.3 f^{-1/2} d_8^{-1/2}$ cm^{-3}. So, the pressure in the hot intercloud gas, $p_{\rm icm} \approx 2.3 n_{\rm H} kT \sim 6.7 \times 10^{-9} f^{-1/2} d_8^{-1/2}$ ergs cm^{-3}. Similarly, for region #16, the volume is $\sim 240 d_8^3$ pc^3, the mean gas density is $\sim 1.1 f^{-1/2} d_8^{-1/2}$ cm^{-3}, and the gas pressure is $p_{\rm icm} \sim 2.1 \times 10^{-9} f^{-1/2} d_8^{-1/2}$ ergs cm^{-3}. Such gas pressures are consistent with the that estimated for the maser portions, $p_{\rm cl} = n_{\rm H_2} kT \sim 0.07$–$8.6 \times 10^{-9}$ ergs cm^{-3}. The far-infrared H$_2$O and OH emission lines are found around the SW maser site. They are consistent with the passage of shock wave through dense clumps and the postshock gas is estimated to have a density $\sim 2 \times 10^5$ cm^{-3} and temperature 100–1000 K (Reach & Rho 1998). Such density and temperature are similar to the condition for the maser production, with a pressure range $p_{\rm cl} \sim 2.8 \times 10^{-9}$–$2.8 \times 10^{-8}$ ergs cm^{-3}, comparable to the above pressure estimates for the SW maser region.

3.3. Stellar remnant?

The association of 3C 391 with a dense molecular cloud makes it possible that 3C 391 is the interstellar remnant of the supernova explosion of a massive star, which may also leave behind a compact star as a result of gravitational core collapse. It is thus important to see if there is any evidence for this stellar remnant. We do locate numerous point-like sources within the boundary of the remnant (for example, evident point sources #22 and #26 right in the center, #24 and #32 in the south, etc.) (see Fig.1d and Table 1). However, spectral analysis for these sources cannot be carried out because of the small number of counts.

A bright unresolved source (source #17) appears near the NW rim and seems to be located at the north apex of the NW diffuse hard emission (the blue patch in Fig.1a and Fig.1b). The spectrum of this source extracted from region #5 (with 158 net counts) is better described with a powerlaw than with a bremsstrahlung or a blackbody (see Fig.4 and Table 3). The hydrogen column density obtained is similar to those of other portions of this remnant, so the possibility of the association of this source with the remnant cannot be ruled out. If this source is at the distance of 3C 391, its unabsorbed X-ray luminosity is $\sim 7.0 \times 10^{32} d_8$ ergs s^{-1}. The steep photon index of the possible powerlaw model 2.5-4.5 is higher than the typical indices 1.2-2.2 of active galactic nuclei (Turner & Pounds 1989), but is similar to those of the some "compact central objects" within SNRs (e.g. Pavlov et al. 2002). If the association with the gaseous remnant is true, the stellar remnant may have moved away from its explosion site. If we follow Reynolds & Moffett's assumption that the explosion site is located at the center of the NW half, then the source would have displaced 2' toward the border. Taking an age of $\sim 4 \times 10^3$ yr, then the displacement velocity would be ~ 1100 km s^{-1}. Such a transverse velocity is quite high, but not unreasonable; pulsar proper motion studies have provided evidence that a small population of neutron stars have

velocities in excess of $\gtrsim 1000\,\mathrm{km\,s^{-1}}$ (Lai 2003). For example, the pulsar B2224+65 in the Guitar nebular pulsar has a velocity ~ 800–$1600\,\mathrm{km\,s^{-1}}$ (Chatterjee & Cordes 2004). Since the age used may be an underestimate, a higher remnant age would allow for a lower velocity.

If the unresolved source is an offset pulsar, a trailing pulsar wind nebula might be expected to be present to the south, roughly in the hard emission region (the blue patch mentioned in §2.1). However, the spectrum of the diffuse gas of the blue patch (region #4) is well described by a thermal model (Table 2). If a power law component is added to fit the spectrum, the photon index would be $7.7^{+2.3}_{-2.2}$, too steep to be physically true. Since the spectrum of region #4 is very week below 1.3 keV (Fig.2) and the hydrogen column density is very high ($\sim 4.1 \times 10^{22}\,\mathrm{cm^{-2}}$), this hard region seems to be the diffuse hot gas suffering heavy absorption in soft X-rays.

4. Conclusion

We observed the thermal composite supernova remnant 3C 391 for 60 ks using *Chandra* ACIS-S detector and carried out a detailed spectro-spatial X-ray analysis which results in following conclusions.

1. The southeast-northwest elongated morphology is similar to that previously found in radio and X-ray studies. Faint shell-like X-ray structures appear along the northern and NE boundary and a faint slab appears at the west rim, while on the SW side the diffuse gas seems to expand out of the radio boundary. The X-ray emission is hardened in the NW, consistent with the increase of hydrogen column density from SE to NW, and all the images and spectra show compellingly that the intervening column density is the primary influence on the broad band X-ray appearance of the remnant.

2. This observation unveils a highly clumpy structure in the remnant. The spatially resolved spectral analysis for the small-scale features found that the gas is generally of normal metal abundance and has approached or basically reached ionization equilibrium.

3. Three mechanisms, radiative rim, thermal conduction, and cloudlet evaporation, may all play roles in the X-ray visage of 3C 391 as a "thermal composite" SNR, but there are difficulties with each of them in explaining some physical properties. By comparison, the cloudlet evaporation model can largely explain some important properties such as the highly clumpy structure, the uniform temperature and density distribution almost all over the remnant, and the much lower X-ray emitting gas density than the mean

ambient cloud density. The enhanced emission in both the SE and NW halves as well as the hydrogen column density gradient does not support the projection effect model. The directly measured postshock temperature implies a young age, $\sim 4 \times 10^3$ yr, for the remnant.

4. The postshock gas pressure derived from the NE and SW rims, which harbor maser spots, is consistent with the estimate for the maser regions.

5. An unresolved source on the northwest border is best fitted in spectrum by a power-law, and its position and absorption column density might suggest a possibility for an association with 3C 391.

REFERENCES

Chatterjee, S. & Cordes, J.M. 2004, ApJ, 600, L51

Chen, Y. & Slane, P.O. 2001, ApJ, 563, 202

Cowie, L.L. & McKee, C.F. 1977, ApJ, 211, 135

Cox, D. P., Shelton, R. L., Maciejewski, W., Smith, R. K., Plewa, T., Pawl, A., & Rózyczka, M. 1999, ApJ, 524, 179

Elitzur, M. 1976, ApJ, 203, 124

Frail, D.A., Goss, W.M., Reynoso, E.M., Giacani, E.B., Green, A.J., & Otrupcek, R. 1996, AJ, 111, 1651 Goss, W.M., Winkler, P.F., & Williams, B.F. 1997, AJ, 113, 1379

Green, A. J., Frail, D. A., Goss, W. M., Otrupcek, R. 1997, AJ, 114, 2058

Harrus, I. M., Hughes, J. P., Singh, K. P., Koyama, K., & Asaoka, I. 1997, ApJ, 488, 781

Koo, B.-C. & Heiles, C. 1995, ApJ, 442, 679

Lai, D. 2003, in 3D Signatures of Stellar Explosion, a workshop honoring J.C. Wheeler's 60th Birthday (astro-ph/0312542)

Lockett, P., Gauthier, E., & Elitzur, M., 1999, ApJ, 511, 235

McKee, C.F. & Cowie, L.L. 1975, ApJ, 195, 715

Moffett, D. A., & Reynolds, S. P., 1994, ApJ, 425, 668

Morrison, R., & McCammon, D., 1983, ApJ, 270, 119

Park, S., Hughes, J.P., Slane, P.O., Burrows, D.N., Warren, J.S., Garmire, G.P., & Nousek, J.A. 2003, ApJ, 592, L41

Pavlov, G.G., Sanwal, D., Kiziltan, B., & Garmire, G.P. 2001, ApJ, 559, L131

Petruk, O. 2001, A&A, 371, 267

Reach, W.T., & Rho, J.H., 1996, A&A, 315, L277

——————, 1998, ApJ, 507, L93

——————, 1999, ApJ, 511, 836

————————, 2000, ApJ, 544, 858

Reach, W.T., Rho, J.H., & Jarrett, T.H., 2002, ApJ, 564, 302

Reynolds, S.P., & Moffett, D.A. 1993, AJ, 105, 2226

Rho, J.H., & Petre, R. 1996, ApJ, 467, 698

Rho, J.H., & Petre, R. 1998, ApJ, 503, L167

Rho, J.H., Petre, R., Schlegel, E.M., & Hester, J.J. 1994, ApJ, 430, 757

Shelton, R. L., Cox, D. P., Maciejewski, W., Smith, R. K., Plewa, T., Pawl, A., & Rózyczka, M. 1999, ApJ, 524, 192

Shelton, R. L., Kuntz, K. D., & Petre, R. 2004, ApJ, accepted, astro-ph/0407026

Slane, P., Smith, R., Hughes, J.P., & Petre, R. 2002, ApJ, 564, 284

Spitzer, L. Jr. 1962, Physics of Fully Ionized Gases (New York: Interscience)

Turner, T.J. & Pounds, K.A. 1989, MNRAS, 240, 833

Wang, Q.D., Chaves, T., & Irwin, J.A. 2003, ApJ, 598, 969

Wang, Z.R. & Seward, F.D. 1984, ApJ, 279, 705

Wardle, M. 1999, ApJ, 525, L101

Wilner, D.J., Reynolds, S.P., & Moffett, D.A. 1998, ApJ, 115, 247

White, R.L., & Long, K.S. 1991, ApJ, 373, 543

Wolszczan, A., Cordes, J.M., & Dewey, R.J. 1991, ApJ, 372, L99

Xu, J. & Stone, J.M. 1995, ApJ, 454, 172

Yusef-Zadeh, F., Wardle, M., Rho, J., & Sakano, M. 2003, ApJ, 585, 319

Zel'dovich, Ya. B. & Raizer, Yu. M. 1967, Physics of shock waves and high-temperature hydrodynamic phenomena (New York: Academic Press)

Table 1.   *Chandra* List of Point-like Sources on S3 Chip

Source No.	CXO No.	δ_x ($''$)	log(P)	Count Rate (10^{-3} cts s^{-1})	HR
(1)	(2)	(3)	(4)	(5)	(6)
1	J184915.0-005651	0.3	-15.0	0.94 ± 0.14	0.86 ± 0.09
2	J184916.1-005827	0.3	-15.0	0.43 ± 0.09	$-$
3	J184916.2-005624	0.4	-15.0	0.47 ± 0.10	0.99 ± 0.11
4	J184916.8-005841	0.5	-11.2	0.20 ± 0.07	$-$
5	J184917.0-005701	0.7	-9.1	0.24 ± 0.07	$-$
6	J184917.4-005710	0.4	-15.0	0.41 ± 0.09	$-$
7	J184917.4-005625	0.6	-13.4	0.30 ± 0.08	$-$
8[a]	J184917.5-005900	0.4	-7.3	0.19 ± 0.07	$-$
9	J184918.9-005252	1.0	-9.1	0.33 ± 0.09	$-$
10	J184919.0-005749	0.3	-15.0	0.33 ± 0.08	$-$
11[a]	J184920.4-005928	0.5	-7.5	0.13 ± 0.06	$-$
12[a]	J184921.1-005357	0.7	-7.0	0.53 ± 0.13	$-$
13[a]	J184921.5-005413	0.6	-7.0	0.44 ± 0.12	$-$
14[a]	J184921.6-005355	0.6	-9.3	0.59 ± 0.14	$-$
15[a]	J184921.9-005351	0.6	-7.2	0.48 ± 0.13	$-$
16[a]	J184922.0-005946	0.8	-7.8	0.14 ± 0.06	$-$
17[a]	J184922.3-005334	0.3	-15.0	2.11 ± 0.21	0.49 ± 0.09
18	J184922.6-005458	0.5	-9.9	0.49 ± 0.12	0.92 ± 0.13
19[a]	J184923.1-005736	0.5	-8.7	0.22 ± 0.07	$-$
20	J184923.7-005705	0.3	-10.5	0.27 ± 0.08	$-$
21	J184924.5-005447	0.5	-9.3	0.47 ± 0.11	$-$
22	J184925.0-005628	0.2	-15.0	1.22 ± 0.16	0.57 ± 0.11
23	J184925.5-005344	0.5	-15.0	0.64 ± 0.13	$-$
24	J184925.7-005749	0.2	-15.0	0.65 ± 0.11	0.87 ± 0.11
25	J184926.1-010024	0.4	-15.0	0.46 ± 0.10	$-$
26	J184927.0-005640	0.2	-15.0	1.16 ± 0.15	0.69 ± 0.10
27[a]	J184927.0-005410	0.5	-8.2	0.66 ± 0.16	$-$
28[a]	J184927.4-005349	0.5	-9.5	0.53 ± 0.13	$-$
29	J184927.8-005318	0.8	-9.2	0.46 ± 0.11	$-$
30[a]	J184927.9-005330	0.7	-8.2	0.42 ± 0.11	$-$
31[a]	J184928.3-005734	0.4	-8.9	0.27 ± 0.08	$-$
32	J184929.1-005741	0.2	-15.0	0.97 ± 0.14	0.75 ± 0.11
33	J184929.4-005951	0.6	-15.0	0.22 ± 0.07	$-$
34	J184929.5-005905	0.3	-15.0	0.52 ± 0.10	1.00 ± 0.10
35[a]	J184931.3-005924	0.6	-7.1	0.22 ± 0.08	$-$

Table 1—Continued

Source No.	CXO No.	δ_x ($''$)	log(P)	Count Rate (10^{-3} cts s^{-1})	HR
(1)	(2)	(3)	(4)	(5)	(6)
36[a]	J184932.7-005805	0.5	-7.7	0.32 ± 0.09	–
37	J184933.9-005406	0.9	-10.0	0.23 ± 0.08	–
38	J184934.4-005238	0.9	-11.4	0.56 ± 0.12	–
39	J184937.0-005825	0.4	-12.7	0.58 ± 0.12	–
40[a]	J184937.3-005438	1.3	-8.3	0.32 ± 0.09	–
41[a]	J184938.5-005848	0.4	-13.1	0.87 ± 0.16	0.78 ± 0.14
42[a]	J184938.6-005629	0.5	-10.2	0.79 ± 0.16	0.86 ± 0.15
43[a]	J184938.6-005845	0.4	-10.1	1.03 ± 0.18	0.78 ± 0.13
44[a]	J184939.6-005820	0.4	-12.2	0.91 ± 0.16	0.64 ± 0.14
45	J184939.7-005721	0.6	-12.4	0.42 ± 0.10	1.00 ± 0.16
46[a]	J184939.7-005817	0.5	-10.2	0.74 ± 0.15	0.75 ± 0.15
47[a]	J184939.8-005849	0.5	-9.6	1.39 ± 0.20	0.35 ± 0.13
48	J184939.9-005532	0.4	-15.0	0.72 ± 0.12	–
49[a]	J184940.0-005848	0.3	-15.0	1.77 ± 0.21	0.51 ± 0.10
50[a]	J184940.0-005643	0.3	-15.0	1.93 ± 0.23	0.30 ± 0.11
51	J184941.4-005441	0.9	-10.9	0.51 ± 0.11	0.86 ± 0.14
52	J184944.7-005428	0.4	-15.0	2.95 ± 0.25	–

Note. — Column (1): Generic source number. (2): *Chandra* X-ray Observatory (unregistered) source name, following the *Chandra* naming convention and the IAU Recommendation for Nomenclature (e.g., http://cdsweb.u-strasbg.fr/iau-spec.html). (3): Position uncertainty (1σ) in units of arcsec. (4): The false detection probability P that the detected number of counts may result from the Poisson fluctuation of the local background within the detection aperture [log(P) smaller than -20.0 is set to -20.0]. (5): On-axis (exposure-corrected) source count rate in the 0.3-7 keV band. (6): The hardness ratio defined as HR $= (H - S)/(H + S)$, where S and H are the net source count rates in the 0.3–1.5 and 1.5–7 keV bands, respectively. The hardness ratios are calculated only for sources with individual signal-to-noise ratios greater than 4 in the broad band (B=S+H), and only the values with uncertainties less than 0.2 are included.

[a] These sources are not removed for spectral analysis, either because of high log(P) (we define a threshold > -9.0) or high possibility of being clumps of diffuse emission (judged by eyes).

Table 2. VNEI fitting results with the 90% confidence ranges and estimates of the gas density

regions	net count rate $(10^{-2}\,\mathrm{cts\,s^{-1}})$	χ^2/d.o.f.	N_{H} $(10^{22}\,\mathrm{cm^{-2}})$	kT_x (keV)	$n_e t$ $(10^{11}\,\mathrm{cm^{-3}\,s})$	$f n_e n_{\mathrm{H}} V / d_8^2$ [a] $(10^{57}\,\mathrm{cm^{-3}})$	$F^{(0)}(0.5\text{-}10\,\mathrm{keV})$ $(10^{-11}\,\mathrm{ergs\,cm^{-2}\,s^{-1}})$	$n_{\mathrm{H}}/f^{-1/2}d_8^{-1/2}$ $(\mathrm{cm^{-3}})$
1	3.88 ± 0.08	90.5/65	2.8 ± 0.1	$0.67^{+0.02}_{-0.04}$	> 200	$2.55^{+0.27}_{-0.53}$	0.84	18
2	4.80 ± 0.09	87.0/79	2.7 ± 0.1	$0.58^{+0.06}_{-0.05}$	$5.1^{+4.6}_{-1.3}$	$3.84^{+1.33}_{-0.89}$	1.31	11
3	2.49 ± 0.07	68.8/48	3.4 ± 0.2	$0.56^{+0.06}_{-0.09}$	> 6.4	$3.46^{+2.08}_{-0.90}$	1.05	6.4
4[b]	4.57 ± 0.09	108.9/79	$4.1^{+0.3}_{-0.2}$	$0.62^{+0.04}_{-0.05}$	> 30	$9.42^{+3.10}_{-2.33}$	2.95	4.8
				([Mg/H]$=1.12^{+0.13}_{-0.09}$, [Si/H]$=0.87^{+0.08}_{-0.05}$, [S/H]$=0.80^{+0.13}_{-0.09}$)				
6	3.30 ± 0.08	65.2/58	$2.7^{+0.2}_{-0.1}$	$0.56^{+0.08}_{-0.06}$	$5.0^{+3.8}_{-2.1}$	$3.20^{+1.41}_{-0.98}$	0.97	6.1
7	3.31 ± 0.08	57.8/58	$3.0^{+0.1}_{-0.2}$	$0.54^{+0.05}_{-0.06}$	> 5.5	$3.97^{+1.65}_{-0.98}$	1.20	6.8
8	3.08 ± 0.07	72.4/52	$2.9^{+0.2}_{-0.1}$	$0.63^{+0.08}_{-0.07}$	> 3.4	$2.52^{+0.60}_{-0.65}$	0.95	5.4
9	2.23 ± 0.06	58.2/43	2.9 ± 0.2	$0.63^{+0.07}_{-0.11}$	> 2.7	$1.72^{+1.35}_{-0.41}$	0.62	4.5
10	2.14 ± 0.06	44.2/44	$3.0^{+0.2}_{-0.1}$	$0.79^{+0.14}_{-0.10}$	$3.1^{+3.6}_{-1.4}$	$1.16^{+0.52}_{-0.34}$	0.40	2.3
11	3.64 ± 0.09	96.9/72	2.8 ± 0.1	$0.59^{+0.06}_{-0.04}$	> 3.8	$3.17^{+0.38}_{-0.77}$	0.94	1.9
12	1.41 ± 0.05	49.8/32	$3.7^{+0.6}_{-0.4}$	$0.58^{+0.11}_{-0.12}$	> 265	$2.28^{+3.19}_{-0.96}$	0.68	2.0
13	4.71 ± 0.10	107.0/82	$3.0^{+0.2}_{-0.1}$	$0.46^{+0.04}_{-0.03}$	> 106	$8.23^{+2.73}_{-2.12}$	2.27	2.6
14[b]	31.3 ± 0.2	273.6/180	2.9 ± 0.1	0.55 ± 0.02	> 9.0	$35.00^{+3.75}_{-5.38}$	10.8	2.9
				([Mg/H]$=1.12^{+0.13}_{-0.09}$, [Si/H]$=0.87^{+0.08}_{-0.05}$, [S/H]$=0.80^{+0.13}_{-0.09}$)				
15[b]	16.3 ± 0.2	237.8/163	3.5 ± 0.1	$0.54^{+0.02}_{-0.01}$	> 23	$34.08^{+5.42}_{-4.20}$	10.2	2.8
				([Mg/H]$=0.92^{+0.14}_{-0.13}$, [Si/H]$=0.53 \pm 0.05$, [S/H]$=0.64^{+0.12}_{-0.11}$)				
16[b]	6.08 ± 0.13	156.3/127	3.2 ± 0.2	$0.53^{+0.04}_{-0.06}$	> 239	$10.0^{+5.42}_{-2.60}$	2.94	1.1
				([Mg/H]$=0.93^{+0.28}_{-0.26}$, [Si/H]$=0.54^{+0.12}_{-0.11}$, [S/H]$=0.54^{+0.24}_{-0.21}$)				
17[b]	112.0 ± 0.5	710.5/296	3.1 ± 0.1	0.56 ± 0.01	> 12.8	150 ± 10	45.5	1.9
				([Mg/H]$=0.97^{+0.07}_{-0.05}$, [Si/H]$=0.70 \pm 0.03$, [S/H]$=0.71^{+0.06}_{-0.05}$)				

Note. —

[a] f denotes the filling factor of the hot gas.

[b] Thawing metal abundances apparently improves fitting.

Table 3.   Spectral fitting results for the NW unresolved source with the 90% confidence ranges

regions	net count rate (10^{-3} cts s^{-1})	model	χ^2/d.o.f.	N_{H} (10^{22} cm^{-2})	photon index	kT (keV)	$F^{(0)}$(0.5-10 keV) (10^{-14} ergs cm^{-2} s^{-1}
5	2.60 ± 0.20 (1–10 keV)	power	4.08/4	$2.6^{+1.4}_{-1.0}$	$3.2^{+1.3}_{-0.7}$	$\cdots$	9.1
		bremsstrahlung	4.86/4	$1.8^{+0.9}_{-0.8}$	$\cdots$	$2.2^{+1.4}_{-0.9}$	5.5
		blackbody	6.95/4	$0.6^{+0.9}_{-0.6}$	$\cdots$	$0.75^{+0.15}_{-0.17}$	3.3

5. Figure captions

Fig. 1.— *Panal a*: Tri-color X-ray image of 3C 391. The X-ray intensity in the 0.3-1.5, 1.5-3.0, and 3.0-7.0 keV bands are color coded in red, green, and blue, respectively. The overlaid 1.5 GHz radio contours are at 1.5, 3, 6, 9, 12, 18, 30, and 45×10^{-3} Jy beam^{-1} (from Moffett & Reynolds [1994]). *Panel b*: Tri-color X-ray + radio image of 3C391. The 1.5 GHz emission is plotted in red, the 0.3-3.0 keV emission is in green, and 3.0-7.0 keV is in blue. *Panel c*: The broad band (0.3-7.0 keV) X-ray image overlaid with 1.5 GHz radio contours (with the same levels described for the top panel). All the X-ray maps used here are exposure-corrected and are adaptively smoothed to achieve a S/N ratio of 3 (using the CIAO program CSMOOTH). The two cross labels in each panel denote the OH maser points (Frail et al. 1996). *Panel d*: Diffuse emission from SNR 3C 391 in the broad band 0.3-7.0 keV. The image is smoothed adaptively with a Gaussian kernel, which is adjusted to a count-to-noise ratio of 6. The color is scaled in the range from $(1.19–331.85) \times 10^{-2}$ ct s^{-1} arcmin^{-2}, logarithmically. The location of the sources removed from the data before the smoothing are marked by crosses. All the regions used for extracting spectra are indicated in blue, with cyan numerical labels. The dashed lines denote the border of the S3 chip.

Fig. 2.— *Chandra* ACIS spectra of 12 small scale emission regions in 3C 391 fitted with the VNEI model. The region numbers, together with the factors multiplying the real fluxes, are labeled on the right side of the spectra.

Fig. 3.— *Chandra* ACIS spectra of the medium-scale emission regions and entire remnant of 3C 391. The region numbers are labelled in each panel.

Fig. 4.— *Chandra* ACIS spectrum of the NW unresolved source (region #5) fitted with the powerlaw model.
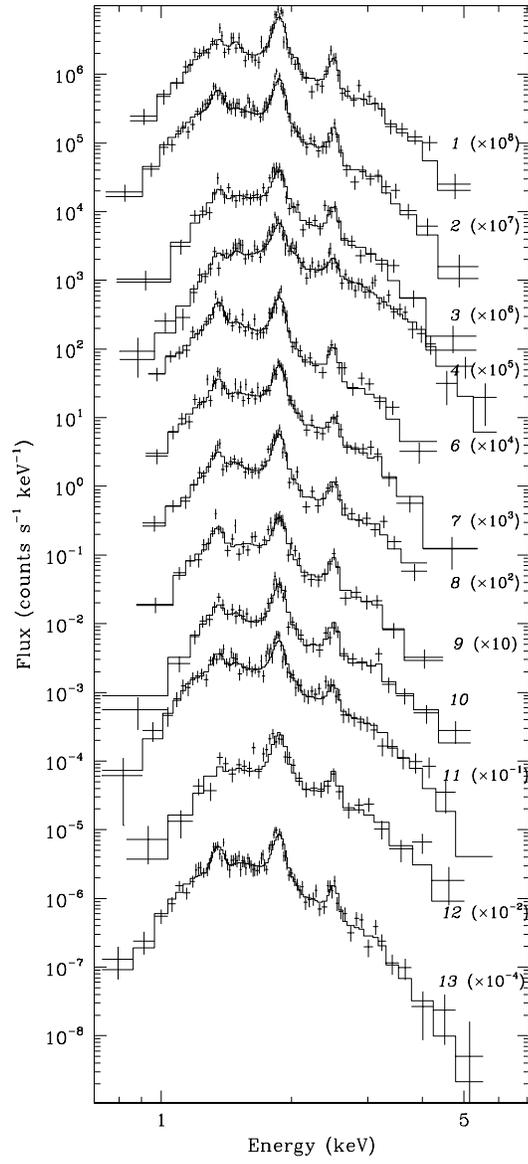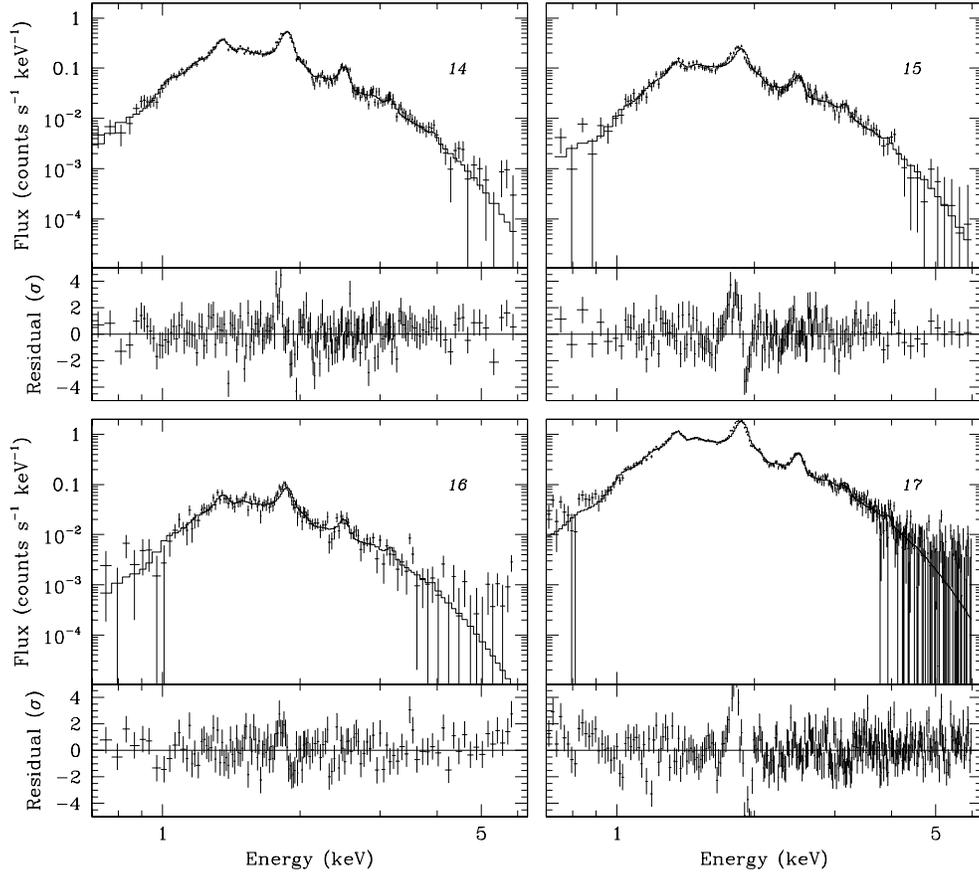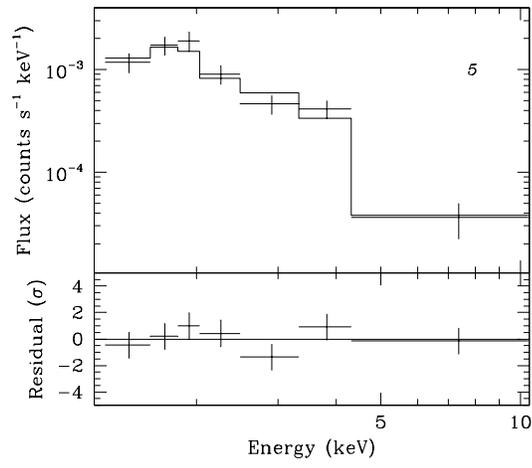
Fig.1 (f1.jpg)

Fig.2

Fig.3

Fig.4

This figure "f1.jpg" is available in "jpg" format from:

http://arXiv.org/ps/astro-ph/0408355v1